PBS	Item	Total Labor [k€]
13.6.9.1	Beam Transport and Conditioning System	1 668,478
13.6.9.2	Sample Exposure System	218,568
13.6.9.3	Scattering Characterization System	183,435
13.6.9.4	Optical Cave	0,000
13.6.9.5	Experimental Cave	287,352
13.6.9.6	Control Hutch	36,456
13.6.9.7	Sampe Preparation Area	15,136
13.6.9.8	Utilities Distribution	5,640
13.6.9.9.1	Support Infrastructure - Hall 1	65,520
13.6.9.10.1	Control Racks - Hall 1	421,640
13.6.9.11	Integrated Control and Monitoring	0,000
	Travel Costs	81,000
	R&D Selene Guide	150,500
	Phase 1	480,000

Total Initial Construction Costs (O2) **3 613,725**

Total non-Labor [k€]	Both [k€]	Both + 10% Contingency [k€]
4 751,999	6 420,477	7 133,863
372,430	590,998	656,664
521,000	704,435	782,706
0,000	0,000	0,000
665,000	952,352	1 058,169
71,000	107,456	119,396
11,160	26,296	29,218
28,000	33,640	37,378
180,000	245,520	272,800
146,265	567,905	631,006
0,000	0,000	0,000
0,000	81,000	90,000
209,500	360,000	400,000
50,000	530,000	588,889
7 006,354	**10 620,079**	**11 800,088**

Work 02 [y]	Work 03 [y]	Work 04 [y]	Work 05 [y]
0,97	4,58	3,08	3,39
0,11	0,64	0,39	0,29
0,20	0,46	0,40	0,36
0,00	0,00	0,00	0,00
0,19	0,80	0,18	1,20
0,07	0,04	0,07	0,18
0,02	0,03	0,00	0,11
0,02	0,03	0,00	0,00
0,03	0,19	0,00	0,29
0,22	1,16	0,09	1,94
0,00	0,00	0,00	0,00
1,830	**7,958**	**4,205**	**7,754**

Work 06 [y]	Total [y]
2,01	14,03
0,34	1,78
0,22	1,65
0,00	0,00
0,09	2,45
0,01	0,37
0,00	0,16
0,00	0,05
0,13	0,64
0,61	4,02
0,00	0,00
	3,25
3,412	**28,408**

Estia DMSC Software Requirements

Artur Glavic and Jochen Stahn

September 17, 2015

Contents

1. High Level Software Requirements **3**
- 1.1. Day 1 of hot commissioning . . . 3
- 1.2. Day 1 for friendly users . . . 3
- 1.3. Day 1 for real operation . . . 3
- 1.4. Beyond . . . 4

2. Overview of Data Analysis Tools **5**
- 2.1. Currently used software for data analysis . . . 5
  - 2.1.1. Basic data analysis concept for reflectometry . . . 5
  - 2.1.2. Data reduction at beamline 4A of SNS . . . 5
  - 2.1.3. Data reduction of Selene measurements at AMOR of SINQ . . . 6
- 2.2. Missing analysis tools . . . 6
- 2.3. Points for improvement in currently used software . . . 6
  - 2.3.1. Live data reduction . . . 6
  - 2.3.2. Synergy between instrument planning and data reduction . . . 6
  - 2.3.3. Connection to modeling software . . . 6
  - 2.3.4. Refinement servers . . . 7
  - 2.3.5. Error estimation . . . 7
- 2.4. Instrument specific aspects . . . 7
  - 2.4.1. Data normalization . . . 7
  - 2.4.2. Resolution function . . . 7
  - 2.4.3. Flexible q-binning . . . 7

3. Concepts of Operation **9**
- 3.1. Geometry . . . 9
- 3.2. Estia operation modes . . . 9
  - 3.2.1. Almost conventional reflectivity . . . 9
  - 3.2.2. λ-θ-encoding . . . 10
  - 3.2.3. High intensity mode . . . 14
- 3.3. Measurement examples . . . 17

A. Appendix 1 **18**
- A.1. List of reflectivity simulation software . . . 18

1. High Level Software Requirements

1.1. Day 1 of hot commissioning

- Raw data view λ vs. θ
- Raw data view horizontal vs. vertical
- Normalization and reduction of reflectivity measurements of high intensity and almost conventional mode
- Scaling of datasets
- Export of reflectivity curves with correct intensity errors
- Script access to data analysis

1.2. Day 1 for friendly users

- Basic user interface to allow specification of data reduction parameters
- Correct calculation of $q_z$errors
- Reduction of reflectivity measured in λ-θ-encoding mode
- Flexible advanced options for normalization parameters

1.3. Day 1 for real operation

- Improved user interface with basic automation options
- Live data reduction
- Reduction of off-specular scattering measured in almost conventional and λ-θ-encoding modes
- Integration of experiment planning software parameters into reduction
- Basic automatic reduction for typical experiments
- Excess to refinement software/dedicated refinement server

1.4. Beyond

- Integration of modeling software
- Parameter error estimation
- Full integration with instrument planning and control software
- Reduction of GISANS datasets

2. Overview of Data Analysis Tools

2.1. Currently used software for data analysis (AMOR@SINQ/BL4A@SNS)

2.1.1. Basic data analysis concept for reflectometry

For most neutron reflectometers the data analysis consists of three basic steps:

Raw data view The instrument and reduction software must allow to view raw data of the measurements in different sensible projections. The basic functionality includes a time-of-flight vs. horizontal detector pixel and horizontal vs. vertical detector pixel map. Further helpful views include a translation of the axes mentioned to wavelength λ and angle θ as well as viewing normalized datasets.

Reduction The raw neutron event data needs to be converted from angle/time-of-flight coordinates into wave vector transfer (q_z), binned, properly normalized and combined to produce a reflectivity curve R(q_z). This reduction step strongly depends on the mode of operation of the instrument and is therefore often done with instrument specific programs. To generate correct reflectivity curves several parameters of the instrument geometry need to be taken into account.

For *Estia* the normalization and binning can become much more complicated than for other time-of-flight machines due to the additional complexity of the high intensity mode described in section 3.2.3.

Modeling Sample models are used to simulate reflectivity curves and refine sample parameters. These simulations mostly use the Parratt[2] recursion or matrix[3–5] formalisms to self-consistently model the refraction and reflection of the wave at the various interfaces in the sample. There is a variety of tools available that implement these models, see a list in section A.1.

2.1.2. Data reduction at beamline 4A of SNS

The magnetism reflectometer uses the python based QuickNXS[1] reduction program with graphical user interface. It allows the normalization and stitching of several time-of-flight based measurements and is optimized for easy usability. The program does reduction of reflectivity, off-specular scattering and GISANS measurements for polarized measurements. Scripting options are limited and there is no support for more than one θ value per file. The raw data views of the GUI mimic the ones used in the instrument control software (dcomclient).

ISIS and SNS are planning to incorporate a QuickNXS based interface into the Mantid framework. In the current stage the program is not instrument independent.

2.1.3. Data reduction of Selene measurements at AMOR of SINQ

At the AMOR instrument at SINQ user experiments are already employing the Selene guide prototype for many measurements. Right now the data reduction is performed with pearl scripts (amorreducer, selenereducer), which perform the normalization of datasets. The output data can be used to look at the raw data against various axes and with different normalization stages.

The scripts are limited to command line operation and the current SINQ data acquisition model does not allow event mode operation or treatment of polarization states. As the mode of operation is very new the analysis script is still under active development and testing. It can be expected that several aspects of the data treatment algorithm needs to be changed during the *Estia* development phase and beyond.

2.2. Missing analysis tools

As the important steps for data reduction is the only analysis tool necessary for reflectometry there is no need for additional tools, only improvement of the currently used procedures.

2.3. Points for improvement in currently used software

2.3.1. Live data reduction

Especially with the decreased measurement times expected at ESS it is essential to quickly generate reflectivity curves to be able to decide on future experimental steps. The currently used data reduction at SNS and SINQ do not allow access to live data and therefore lead to unnecessary delays of such decisions.

2.3.2. Synergy between instrument planning and data reduction

Many parameters necessary for the data reduction are already known during the planning of the experimental script. One example would be the mapping of run numbers to individual reflectivity measurements. This aspect could be used to speed up the reduction process by recording such information to the data files during acquisition.

2.3.3. Connection to modeling software

Some of the reflectivity programs allow expansion through plugins (e.g. GenX), which could be used to form a connection to the data reduction software. This could be used to quickly refine the recorded spectra, especially in combination with live data. This

way the refinement could be improved while data is recorded and after the measurement is finished the results would instantly be available.

2.3.4. Refinement servers

Large amounts of measurement data necessitates quick refinement. Although reflectivity data generally can be fitted with a normal personal computer, a dedicated refinement server would be necessary for sets of e.g. parameter dependent reflectivity measurements.

2.3.5. Error estimation

Least squares refinement of reflectivities is often done with non-linear weighting as the information about the sample structure is within oscillations that drop after the cricical edge of total reflection with $\approx q_z^{-4}$. Up to now it has been hard to estimate actual errors on the retrieved model parameters/scattering length density profiles. Mathieu Doucet at SNS data analysis is investigating a Monte-Carlo based method of varying starting parameters and data points to help with this estimation. This effort could be picked up for ESS reflectometer, as well, as it is instrument independent.

2.4. Instrument specific aspects

2.4.1. Data normalization

Especially *Estia*'s high intensity mode requires a more complicated treatment during data reduction. The 2D data needs to be binned into $q_z$ranges and normalized by some kind of incident spectrum measurement. This incident spectrum could be a direct beam or super-mirror measurement. Depending on the measurement conditions of these reference spectra the data normalization is performed differently (a direct beam measurement has inverse θ direction on the detector, super-mirrors have a $q_z$dependent intensity).

The software needs to be flexible enough to allow certain instrument parameters to be overwritten (e.g. wrong θ calibration during measurement) while at the same time allowing quick reduction of standard measurements for users.

2.4.2. Resolution function

The resolution of individual points on the reflectivity will be λ and θ dependent. The reduction process must be able to correctly calculate these resolutions as they are used in the simulation programs and can considerably change the model.

2.4.3. Flexible q-binning

As reflectivity datasets span a large intensity range and the same $q_z$will be measured with different wavelengths and angles in the high intensity mode, a constant $\frac{\Delta q_z}{q_z}$

binning will not produce the optimal results possible. A flexible binning based on measured intensity would allow to have the best point resolution while keeping the statistics as necessary.

Another option would be to directly model the measured data using the known resolution function. This option would approximately square the number of necessary calculation points and therefore have considerable performance impact.

3. Concepts of Operation

3.1. Geometry

«Filled in later.»

3.2. Estia operation modes

3.2.1. Almost conventional reflectivity

measurement scheme This mode corresponds to the conventional TOF reflectometry, where the beam divergence and footprint size are defined by slits. The angle of incidence and the divergence are constant for the duration of one pulse. Using the *Selene* guide the footprint is defined by the virtual source. For adjusting the divergence one slit (the aperture) behind the last guide element is sufficient.

Due to the analogy with conventional TOF reflectometers, the data collection, normalisation and further treatment for one angle of incidence follow exactly the procedure used there.

An additional feature when using a wide divergence cut down by a narrow aperture is that by moving this aperture in between measurements, one can change θ without rotating the sample.

Figure 3.1.: Sketch to illustrate the operation scheme: the beam (gold) is transported with the full divergence and without chopping to the end of the guide system. There an aperture (black) defines $\Delta\theta$, and its position together with the sample orientation ω also the angle of incidence θ. The beam footprint on the sample is defined by size and orientation of the virtual source.

Data acquisition

The width of the q_z-range covered in one measurement with constant θ is rather small (given by $\lambda_{\max}/\lambda_{\min} = 1.88$). Thus in most cases several sample orientations are needed, which results in longer measurement times due to the movement of the detector. A possible combination of angles of incidence θ with 4% overlap is given in table 3.1.

The wide divergence of the incoming beam opens the opportunity to cover the first 4 angles by moving the aperture rather than by rocking sample and detector. The

$\frac{q_z}{-1}$	$\frac{\theta}{\text{deg}}$	$\frac{\omega}{\text{deg}}$	$\frac{\omega}{\text{deg}}$	$\frac{\text{offset}}{\text{deg}}$
0.005 → 0.009	0.21	−1.04	−0.40	−0.64
0.009 → 0.017	0.39	−0.86		−0.46
0.016 → 0.030	0.69	−0.56		−0.16
0.029 → 0.055	1.25	0.00		+0.40
0.052 → 0.099	2.25	1.00		
0.094 → 0.178	4.05	2.80		
0.170 → 0.320	7.29	6.04		
0.306 → 0.575	13.12	11.87		
0.551 → 1.036	23.62	22.37		

Table 3.1.: q_z-ranges covered with one sample orientation. The third column gives the corresponding angle of incidence θ and the forth column the sample tilting with respect to the long half axis of the *Selene* guide, ω. The wide divergence of the beam incident on the aperture allows within limits for changing θ by moving the aperture. This is illustrated in columns 5 (ω) and 6 (offset of the aperture). The limit for the offset is $\pm 0.75°$.

actual counting times will stay the same, but the switching between the settings is much faster (a few pulses might be lost by repositioning the aperture).

Discussion

This is the method of choice if off-specular scattering is to be measured, or in cases when the background caused by off-specular or diffuse scattering has to be separated or reduced.

The performance of *Estia* in this mode is expected to be very close to other concepts since the beam intensity and thus the measurement times are essentially given by the brilliance transfer of the guide.

The instrument-intrinsic resolution $\Delta\lambda/\lambda$ varying from 2% to 4% between 9.4 and 5 leads to a saw-tooth-like shape of the resolution function of the full measurement (see figure **??** d). For all measurements requiring moderate to low resolution (which is the by far largest fraction) this is completely fine **??**. For higher resolution the λ-θ-encoding mode described in the next section has to be chosen.

3.2.2. λ-θ-encoding

The strengths of the λ-θ-encoding are the wider q_z-range accessible with one angular setting, a possible constant $\Delta q/q$, and eventually the *nicer* off-specular area, compared to the almost conventional mode.

the measurement scheme There are (at least) two possibilities to obtain a λ-θ-encoding: either by using the pulsed structure and varying the angle of incidence θ with time - and thus with λ. Or to spectraly analyse the beam (no pulsed beam is needed) e.g. by reflecting on a multilayer monochromator, or by refraction using a prism [**?**].

Figure 3.2.: Sketch to illustrate the operation scheme: the beam (gold) is transported with the full divergence and without chopping to the end of the guide system. As in the conventional mode **??**, a slit (black) defines $\Delta\theta$ and together with the sample orientation ω also the angle of incidence θ. But the opening and position change during the passing of each pulse. This way high θ can be related to low λ and vice versa.

scanning aperture The divergence-defining aperture behind the guide exit scans across the convergent beam in the direction of the sample normal for each pulse and thus creates a λ-θ-encoding. Figure 3.2 shows the principle. The aperture position defines $\theta(\lambda \propto t)$. For covering a wide q_z-range it should be located at the high-θ edge at the time the 5 neutrons arrive and at the low-θ edge for 9.4 . The aperture opening defines $\Delta\theta$. Thus a variation of the slit-width Δy with time can be used to realise $\Delta\theta/\theta = \text{const}$, or more sophisticated, $\Delta q/q = \sqrt{(\Delta\lambda/\lambda)^2 + (\Delta\theta/\theta)^2} = \text{const}$, where $\Delta\lambda = \text{const} \approx 0.2$ here.[1]

As long as both blades forming the aperture are in one plane, the resolution $\Delta\lambda/\lambda$ is not affected. By separating the blades along the flight direction x one can realise a set-up analogue to the blind double chopper concept by Ad van Well [**?**]. Looking at one neutron trajectory (and assuming a continuous beam for the beginning), the two blades create a pulse with $\Delta\lambda/\lambda = \Delta x_\mathrm{a}/x_\mathrm{ad} = \text{const}$, where x_ad is the distance from the aperture mid-point to the detector, and Δx_a is the separation of the blades. The same is true for any trajectory as long as the edges of the blades are exactly in line with the sample at all times. I.e. they move with slightly different speeds. With the continuous beam this is a TOF set-up with time-zero varying with angle of incidence θ. With the pulsed beam and coupling θ to λ the band-width of the beam arriving at the aperture is restricted to $\Delta\lambda = 0.2$, which is the resolution of the encoding. The latter affects only the off-specular resolution of the measurement.

Given the intrinsic resolution of $\leq 4\%$, a constant $\Delta\lambda/\lambda$ is only useful for 1% or 2%, which corresponds to a separation $\Delta x_\mathrm{a} = 84\,\mathrm{mm}$, or 168 mm, respectively.

spectral analysis using a multilayer A ML monochromator at or before the virtual source encodes the wavelengths of the neutrons in the final angle of the monochroma-

[1] Solving this equation for $\Delta\theta$ gives (l is the slit-sample distance):

$$\begin{aligned}
\Delta\theta(t) &= \theta(t)\sqrt{\left(\frac{\Delta q}{q}\right)^2 - \frac{\Delta\lambda^2}{(\lambda_\mathrm{min} + (\lambda_\mathrm{max} - \lambda_\mathrm{min})(\theta(t) - \omega + \epsilon)/\Delta\theta_\mathrm{beam})^2}} \\
&\approx \arctan\frac{\Delta y(t)}{l} \\
\theta(t) &= \omega + \epsilon + \frac{\Delta\theta_\mathrm{beam}}{2} + \frac{\lambda(t) - \lambda_\mathrm{min}}{\lambda_\mathrm{max} - \lambda_\mathrm{min}}\Delta\theta_\mathrm{beam} \\
&= \omega + \arctan\frac{y(t)}{l}
\end{aligned}$$

Figure 3.3.: Illustration of the principle of the λ-θ-encoding. A convergent white (pulsed) beam is spectral analysed by a ML monochromator (a). The beam then propagates to the sample keeping the relation between λ and θ (b). For a pulsed beam at any time an almost monochromatic beam is impinging on the sample, where θ and $\lambda \sim \theta$ vary with time. The sketches (c) to (e) show snap-shots of the beam within the *Selene* guide system and after the sample. In (f) to (i) the corresponding situation on the sample is shown.

tor.[2] For small θ one gets $\theta \propto \lambda$. The specular reflectivity from the sample then leads to a diagonal streak in $I(\lambda, \theta)$ on the detector, so that off-specular scattering can be measured. Figure 3.3 shows *snap-shots* of the beam-distribution within the guide and at the sample.

The resolution in q_z is essentially given by the ML monochromator and can reach 2%, while the TOF resolution influences Δq_x. So this mode could be realised without any chopper.

The guide geometry, its coating and the wavelength-range define $\Delta\theta$ **??**, i.e. for $\lambda \in [5, 9.4]$ and $\Delta\theta = 1.5°$ one gets $m \approx 3.4$ with $\theta \in [1.7°, 3.2°]$. A plateau of total reflection ($m \leq 1$) results in $\theta \leq 1°$ for the same λ-range. Thus totally reflected neutrons do not reach the guide.

A ML monochromator leads to an illumination of the *off-specular region* on the detector by diffuse and off-specular scattering at the multilayer, but also by specular scattering away from the Bragg condition. This can be seen in figure **??**. The off-specular contribution can be suppressed by the virtual source diaphragm if the monochromator is located before it. An additional scanning aperture the sample (see above) can be used to filter the unwanted specular intensity from the monochromator. This combination allows for a clean beam and a high and constant resolution.

Data acquisition

Also the data acquisition follows the scheme of the almost conventional reflectometry. Only the number of q_z-ranges is reduced, and the counting times are increased. Table 3.2 gives a set of possible orientations ω and the related θ- and q_z-ranges.

Figure 3.4 shows a simulated $I(\lambda, \theta)$-map for $\omega = 5°$. The sample is a Ni/Ti multilayer with artificial off-specular scattering[3] The diagonal specular streak is clearly

[2] In principle one could use the monochromator itself as the virtual source: It has to have the shape and orientation of the sample or smaller for under-illumination. But in this case all scattering from the monochromator, specular and off-specular, is focused to the sample and results in background in the off-specular signal from the sample.

[3] The specular reflectivity was simulated with EDXR [**?**] The off-specular signal is *generated* by convolution of the specular reflectivity $R(q_z)$ with 2 Gaussian functions $R(q_x, q_z) = R(q_z) * (g_1(q_x) + g_2(q_x))$. with a cut-off at the sample horizon. A bending of the Bragg sheets, Yoneda wings and the low-intensity region between Yoneda and horizon are not produced this way. Within McStas this folding is achieved by randomly adding a q_{xy} component, but with a Gaussian probability distribution centred at $q_{xy} = 0$.

ω / deg	$\theta_{\min}$ / deg	$\theta_{\max}$ / deg	$q_{z\,\min}$ / $^{-1}$	$q_{z\,\max}$ / $^{-1}$
−0.4	0.1	1.6	0.003	0.068
1.7	2.2	3.7	0.052	0.160
5.0	5.5	7.0	0.128	0.305
10.0	10.5	12.0	0.253	0.522

Table 3.2.: Sample orientations ω and related θ- and q_z-ranges as used for the simulations shown below.

visible. Its width is given by the opening of the scanning aperture. The Bragg peaks show the resolution for the specular intensity to be oriented along lines originating from $(\lambda = 0, \theta = 0)$. The visible off-specular Bragg-sheets are inclined with respect to these.

Figure 3.4.: Intensity-map $\log_{10}[I(\lambda, \theta)]$ of the NiTi multilayer for $\omega = 5°$. The map is already corrected for $I(\lambda)$ of the incoming beam.

Normalisation and integration

Normalisation for the off-specular region is a bit more complicated than discussed in the general part for specular reflectometry because there is no reference sample with a well-known high-intensity off-specular scattering.

Most likely one has to use the specular reference to also scale the off-specular region, taking inhomogeneities of the detector into account. An alternative, but time-consuming approach is to perform an ω-scan with the reference sample. After illumination correction this mimics an off-specular signal with specular intensity, and the latter is known.

Here, for normalising the simulations a perfect reference sample was assumed, and the *measurement* was repeated without the scanning aperture. Figure 3.5 shows the $I(q_x, q_z)$-maps obtained for the four ω orientations, and figure 3.6 the resulting $R(q_z)$ curves.

Discussion

The λ-θ-encoding mode allows to cover the most often used q_z-ranges with 2 to 4 sample orientations. With the encoding performed by a co-planar scanning aperture the off-specular region up to $q_x \approx \pm 3 \cdot 10^{-3\,-1}$ is accessible. The varying resolution from 2% to 4% for each range results in a mismatch in the overlapping regions. For a consistent data treatment the individual measurements should be convoluted to constant 4% before merging and comparison to a simulated curve.

The main outcome of the simulation is that a good separation of specular and off-specular reflectivity can be reached with the λ-θ-encoding. The number of angular

Figure 3.5.: Intensity-maps $\log_{10}[I(q_x, q_z)]$ of the NiTi multilayer for $\omega = 5°$ (top), and for all sample orientations given in table 3.2, obtained by summation over the individual maps (left). There is no total reflection plateau visible, here. This is a result of the insufficient computing statistics of the presented map.

Figure 3.6.: $R(q_z)$ of the NiTi multilayer, obtained from the maps shown in figure 3.5 with a binning of $\Delta q/q = 1\%$. The green line is the initial reflectivity convoluted to $\Delta q/q = 2\%$. The data set for $\omega = -0.4°$ clearly shows the insufficient computational statistics. The other data points show a systematic tilt to lower intensities for small q_z. This originates from an improper choice of the Gaussian, widening the specular intensity in q_x direction. This width is larger than the 2% resolution used for data analysis, and thus part of the specular intensity is missing.

settings to cover $q_z \in [0.01, 0.5]^{-1}$ is reduced to 4 relative to the conventional mode needing 7 settings (with 10% overlap).

The next step will be to use an aperture with shifted blades, allowing for a constant high resolution (for the cost of longer counting time).

3.2.3. High intensity mode

the measurement scheme The full beam leaving the *Selene* guide is directed to the sample. The reflected beam is measured with an area-sensitive detector, who's distance and resolution defines the angular resolution $\Delta\theta$ (see figure 3.7). Each intensity curve obtained by integrating over the detector normal to the scattering plane for a given position along the scattering vector (i.e. a certain θ) corresponds to one TOF measurement. This is illustrated in figure **??**.

The increase of specularly reflected intensity is about an order of magnitude with respect to the conventional set-up, or with the λ-θ-encoding. The price to be payed

is that the off-specular resolution gets completely lost. The off-specular scattering corresponding to one θ-channel forms a background for all other channels. Most likely there is no way to de-convolve the specular and the off-specular signals.

Figure 3.7.: Sketch to illustrate the high-intensity specular reflectivity operation mode.

Simulation

Data acquisition and reduction is shown below for a simulated experiment. The corresponding real life experiment is discussed in section **??**.

the sample The sample used for this simulations is a multilayer of the composition

$Si(179)$ / $Fe(12)$ / $Cu(462)$ / Si-substrate

The ideal reflectivity was simulated using EDXR [**?**], where the SLD for magnetic Fe was chosen to be $14.096 \cdot 10^{-6\ -2}$ for $Fe^{|+\rangle}$, and $2.096 \cdot 10^{-6\ -2}$ for $Fe^{|-\rangle}$, respectively. No off-specular or incoherent scattering was assumed. The binning is $\Delta q = 4.4 \cdot 10^{-4\ -1}$. The substrate area is $5 \times 5\,\mathrm{mm}^2$.

The sample for this example was inspired by work of B. Wiedemann, TUM, who investigates the magnetic behaviour of thin iron films during growth. According in-situ measurements were performed at REFSANS, MLZ, and on Amor, PSI, using the *Selene* prototype **??**. Feasibility studies for the latter were performed with a sample similar to the one used in these simulations, but with a larger area.[4] Figures **??** and **??** show the experimental raw-data, the reduced $I(\lambda, \theta)$-map and the resulting reflectivity curves.

Data acquisition

To cover $q_z \in [0.01, 1]^{-1}$ there are 6 angular settings necessary (with a large overlap of 20%). The following table gives the sample tilt ω, and the corresponding θ-range and q_z-range.

Figure 3.8 (a) shows the $I(\lambda, \theta)$-map for $\omega = -0.3°$. For normalisation here an ideal supermirror ($R(q_z) = 1 \forall q_z$) was assumed. The corresponding intensity map is shown in figure 3.8. It can be seen there that the highest intensity occurs at low λ and high θ. The first finding results from the choice of the λ-range **??**. The second finding results from the increasing projected sample area for larger θ.

Figure 3.8 (e) shows the simulated $R(q_z)$ data points obtained by projection of $\mathbf{R}(\lambda, \theta)$ onto q_z.

[4] For the off-situ experiments the Fe-layer was prevented from oxidation by covering it with the Si-layer.

ω / deg	$\theta_{\min}$ / deg	$\theta_{\max}$ / deg	$q_{z\,\min}$ / $^{-1}$	$q_{z\,\max}$ / $^{-1}$
−0.3	0.2	1.7	0.005	0.074
1.8	2.3	3.8	0.054	0.166
5.0	5.5	7.0	0.128	0.305
10.0	10.5	12.0	0.253	0.522
17.5	18.0	19.5	0.412	0.834
30.0	30.5	32.0	0.677	1.102

Table 3.3.: Sample orientations ω and related θ- and q_z-ranges for the simulations. The time t is determined by the highest relative error of 14% after re-binning to 2.5%.

Figure 3.8.: Simulated intensity-maps $I(\lambda, \theta)$ for a sample with the composition (a) $Si\,(179\,)\,/\,Fe\,(12\,)\,/Cu\,(462\,)\,/\,Si$ and a size of $5 \times 5\,\mathrm{mm}^2$, and for a perfect supermirror with the sample shape (b), respectively. Map (c) is obtained by pixel-wise division of maps (a) and (b). For map (d) λ was converted to q_z. Integration along θ and re-binning to $\Delta q/q = 2.5\%$ lead to the red marks in diagram (e). The green line is obtained by convolving the initial $R(q_z)$ used for the simulations with $\Delta q/q = 2.5\%$.

The complete procedure was repeated for all ω settings mentioned in table 3.3, and the resulting individual reflectivity curves as well as the merged curve are shown in figure 3.9.

Discussion

counting time The gain of the high-intensity mode over the λ-θ-encoding mode in the present case is a factor 20 for the lowest ω and decreases for increasing ω. The reason is that in the encoding mode $\Delta\theta$ and thus the slit-opening are proportional to θ. At $\omega \approx 30°$ ($\theta \in [30, 5°, 32°]$) the aperture opening corresponds to half the full divergence. The time-gain there is only about a factor 2.

The average reduction in counting time for a moderate q_z-range (up to $\approx 0.5\,^{-1}$) is one order of magnitude.

For larger samples, relaxed resolution (binning) requirements, or lower counting statistics it is possible to reach the split-second time-scale for time-resolved measurements. The q_z-range one can cover in one shot e.g. spans from $0.01\,^{-1}$ to $0.085\,^{-1}$.

resolution Even though the resolution function is quite complex, the final $R(q_z)$ curve follows the simulated curve convoluted with 2.5% resolution up to high q_z. So even without a data treatment as suggested in section **??** a reasonable result is achievable in the high-intensity mode. This is in agreement with the experimental findings obtained with the *Selene* prototype.

dynamic range The dynamic range of 8 orders of magnitude obtained in the simulations is not realistic. The simulations ignored all background from the sample itself,

Figure 3.9.: Specular reflectivity $R(q_z)$ of the multilayer $Si\,(179)\,/\,Fe\,(12)\,/Cu\,(462)\,/\,Si$. The green curves correspond to the ideal reflectivity, convoluted with $\Delta q/q = 2.5\%$, the upper red and blue data points were obtained by simulations in the high-intensity specular mode for various sample orientations ω 3.2.3. These are scaled by 10 for clarity. The lower red data points were obtained by merging the individual *measurements*. The binning has a width of $\Delta q/q = 2.5\%$. The gray curve gives the relative error of the merged $R(q_z)$, the straight gray line is at 0.14.

from the sample environment, and from the detector. And the sample was assumed to show no off-specular or diffuse scattering.

3.3. Measurement examples

«Filled in later.»

A. Appendix 1

A.1. List of reflectivity simulation software

AFIT -

drydoc http://material.fysik.uu.se/Group_members/adrian/drydoc.htm

GenX http://genx.sourceforge.net

Iprof Adrian.Rennie@fysik.uu.se

Motofit http://motofit.sourceforge.net/wiki/index.php/Main_Page

Parratt http://www.hmi.de/bensc/software/index2.html

Reflpak http://www.ncnr.nist.gov/reflpak

slab_fit cubitt@ill.fr

wetdoc/wetlay Adrian.Rennie@fysik.uu.se

Bibliography

[1] A. Glavic. Quicknxs users manual, October 2014.

[2] L. G. Parratt. Surface studies of solids by total reflection of x-rays. *Physical Review*, 95(2):359–, July 1954.

[3] S. A. Stepanov, E. A. Kondrashkina, R. Köhler, D. V. Novikov, G. Materlik, and S. M. Durbin. Dynamical x-ray diffraction of multilayers and superlattices: Recursion matrix extension to grazing angles. *Phys. Rev. B*, 57(8):4829–4841, Feb. 1998.

[4] S. A. Stepanov and S. K. Sinha. X-ray resonant reflection from magnetic multilayers: Recursion matrix algorithm. *Physical Review B*, 61(22):15302–15311, June 2000.

[5] B. P. Toperverg. Specular reflection and off-specular scattering of polarized neutrons. *Physica B: Condensed Matter*, 297(1-4):160–168, Mar. 2001.

Nuclear Instruments and Methods in Physics Research A 821 (2016) 44–54

Contents lists available at ScienceDirect

Nuclear Instruments and Methods in Physics Research A

journal homepage: www.elsevier.com/locate/nima

Focusing neutron reflectometry: Implementation and experience on the TOF-reflectometer Amor

J. Stahn *, A. Glavic

Paul Scherrer Institut, Laboratory for Neutron Scattering and Imaging, 5232 Villigen PSI, Switzerland

ARTICLE INFO

Article history:
Received 30 November 2015
Received in revised form
4 February 2016
Accepted 2 March 2016
Available online 5 March 2016

Keywords:
Reflectometry
Neutron
Focusing

ABSTRACT

Neutron reflectometry is a powerful tool to investigate chemical and magnetic depth profiles near surfaces. The advantages of neutrons compared to x-rays are their sensitivity to isotopes, the high penetration capabilities and the high sensitivity to magnetic induction. The biggest disadvantage however is the low flux available, which leads to much longer counting times on much larger samples.

In order to boost the performance of neutron reflectometers, a focusing guide system was developed and realised over recent years. Here we report on the application and performance of a down-scaled demonstrator of such a *Selene* guide, installed as an add-on on the time-of-flight (TOF) reflectometer Amor at the PSI. Due to the limited size of the guide, the flux is concentrated to a footprint of at most 2 mm width. It is thus possible to avoid illumination of contacts even on small samples. Despite the fact that typical samples measured on Amor with a size of 10×10 mm^2 are markedly under illuminated, the presented set-up leads to a reduction in counting time of 80%. The use of the demonstrator thus allows for in-situ or in-operando investigations with a time resolution of a few minutes for a q_z range from 0.005 Å^{-1} to 0.08 Å^{-1}.

Besides a short recapitulation of the concept of focusing reflectometry, a detailed description of the data reduction and its quality is given, followed by an application example.

1. Introduction

Reflectometry is a method to probe densities of flat samples near the surface. In this paper only the depth-profile (averaged parallel to the surface) is regarded. This means we concentrate on specular reflectometry here. The quantity actually probed and what *near* means depends on the radiation used. In the present case with cold neutrons the reflectivity contains information about the depth profile of the average nuclear (isotope) density and the in-plane magnetic induction. The depth resolution reaches from the sub-nm range up to a fraction of a μm, where the limits are imposed by the measurement range and the instrumental resolution.

The principle is that a defined beam hits the surface under investigation at a grazing angle and is partly transmitted and partly reflected there. The measured quantity is the intensity of the reflected beam, to which the reflectance of the surface and of all the parallel interfaces underneath contribute. In a simplified picture the contrast between the layers defines the amplitude and the thicknesses of the films the phase of the reflected neutron. The measured signal is the result of the interference of all reflected waves. For a quantitative interpretation of the data one has to compare the measured reflectivity to one calculated on the basis of an assumed model. The calculation requires the solution of the wave equation for the neutron interacting with all interfaces simultaneously [1].

The strength of neutrons compared to the much cheaper x-rays is that they are sensitive to light elements and isotopes, have a higher penetration depth, are sensitive to magnetism, and that they can easily penetrate through the sample environment allowing for extreme temperatures, magnetic fields and pressure. This makes them an ideal probe to investigate for example biological membranes, absorbed layers at solid or liquid surfaces, diffusion between layers, magnetic depth profiles in artificial heterostructures or multiferroic films, and many more.

The drawback of neutron reflectometry is that the measurement time is quite long. Depending on the source, the sample size and the scientific question data collection periods range from a few seconds up to a day for one reflectivity curve, seconds are the exception.

In the following we present an approach of how to speed up the measurements by an order of magnitude for small samples, where small means that the sample width is below the achievable beam spot size. In the presented set-up this means a width of

* Corresponding author.
E-mail addresses: jochen.stahn@psi.ch (J. Stahn), artur.glavic@psi.ch (A. Glavic).

http://dx.doi.org/10.1016/j.nima.2016.03.007

2 mm, for a full-scale realisation up to 20 mm can be reached. A detailed description of the experimental set-up and the data reduction is given, followed by an example.

2. Concept of focusing, high-intensity reflectometry

To obtain the specular reflectivity $R(q_z)$ one has to measure the intensity of a beam reflected from a surface with the momentum transfer q_z normal to the surface. There are two conventional approaches to scan $q_z = \frac{4\pi}{\lambda} \sin\theta$. Either the wavelength λ is kept fix and the angle of incidence θ is varied (angle-dispersive set-up) or θ is kept constant and λ is varied (energy-dispersive set-up). The latter is realised by using a pulsed neutron beam, where the travelling time from the pulse generator (the source or a chopper) to the detector is measured. This time is directly proportional to λ. In both setups, the instrumental resolution is determined by the angular resolution σ_θ, given by the slit and sample geometry, and by the wavelength resolution σ_λ, determined by the monochromator or the pulse duration and flight path length.

In order to reduce the counting time for specular reflectometry measurements on continuous sources, R. Cubitt suggested to use a well-collimated white beam incident on the sample and to spectrally analyse the reflected beam by using a refractive prism. A position-sensitive detector is then used to detect the refraction angles and thus the wavelengths. In this RAINBOWS concept [2] the flux gain is proportional to the wavelength band (and the related incident intensity), reduced by the projection of the beam footprint on the sample to the detector. The latter is limited by the prism size and the angular resolution of the set-up.

An other approach is the REFOCUS concept by Ott [3]. He suggested to encode λ in θ in a beam of wide divergence focused to the sample. The impact location of the reflected neutron on the position sensitive detector then is used to obtain θ and in consequence also λ. In this concept the beam is prepared by a planar-elliptic reflector with a graded monochromating coating. This approach would increase the flux on the sample by an order of magnitude. But the resolution function $\sigma_\theta(\lambda)$ as obtained with the suggested graded monochromator is not acceptable. An alternative approach is to use a coating which reflects all wavelengths (up to a technical threshold) and to realise the encoding by reflection of the neutrons on a q_z-bandpass mirror[1] at the initial focal point of the ellipse.

We adapted the idea of using a focused beam and to measure θ with the detector to a time-of-flight instrument. Here no wavelength encoding is necessary for specular reflectometry and thus the full pulsed beam is sent to the sample. This approach sacrifices the ability to measure specular and off-specular reflectivity simultaneously, but the flux gain on the sample for specular measurements is proportional to $\Delta\theta/\sigma_\theta$. This means an increase in flux by more than an order of magnitude for small and moderate q_z, and a bit less for very high q_z.

Most neutron reflectometers are built for small divergences (up to $\approx 0.4^\circ$) and use the approach of defining the beam using a pair of slits (often this is referred to as *focusing*, but slits just cut down the phase space, they do not spatially concentrate flux). This restricts the possible gain factors and the wide opening of the slits necessary for high-intensity specular reflectometry leads to a strong illumination of the sample environment and thus to high background. Thus one needs some optics to deliver a truly focused beam in a sense that only a defined small spot is illuminated and, ideally, not the surrounding area.

[1] A periodic multilayer, normally referred to as *monochromator coating*. This term is not appropriate here because in total a wide wavelength band is reflected.

2.1. The Selene guide

Over recent years we have developed a truly focusing neutron guide system which we called *Selene* guide [4,5]. This attempt was triggered by ideas of Ott [3,6]. Later we found that in 1963 a similar guide was suggested by Maier Leibnitz and Springer [7], but at that time it could not be realised technically. The initial intention was to use it for reflectometry as is described here, but it can also be applied to other purposes as long as the guide length, the wavelength range, the sample size and the requested divergence are within limits imposed by gravity and the available (and affordable) coating of the guides.

This *Selene* guide system is made of two subsequent planar-elliptical reflectors which share the long axis and one focal point. This leads to an imaging system where coma aberration, which is inherent to elliptical mirrors, is corrected to first order. This means that the geometrical properties of the beam at the final focal point (in the presented case the sample position) can be defined at the initial focal point, here referred to as the *virtual source*. When this concept is applied in the horizontal and vertical direction normal to the beam, a 3-dimensional image of the virtual source is projected onto the sample. Fig. 1 illustrates this geometry.

Used for reflectometry, the imaging property means that the beam-footprint on the sample surface is defined a long distance away from the sample. This leaves more flexibility for the sample environment. The maximum divergence of the beam is defined by the emittance of the virtual source and the geometry of the guide. It can be reduced in a defined way by using an aperture at the exit of the guide, still far from the sample. The restriction of the divergence does not affect the footprint, and vice versa.

The *Selene* guide is not to be confused with 4-sided elliptic neutron guides. Those typically have their entrance and exit quite close to the focal points, and they are used on large sources. As a consequence aberration leads to garland and zigzag trajectories in the guide and the geometrically focusing property is largely lost.

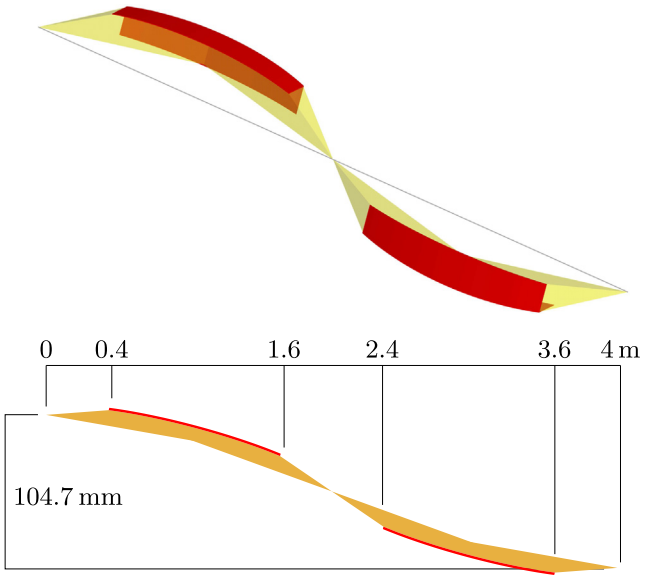

Fig. 1. Illustration of the geometry of a *Selene* guide. The first pair of planar elliptic mirrors (red), mounted at 90°, focuses the neutron beam (yellow) to the intermediate focal point. At this point the beam is strongly affected by coma aberration. The second pair, oriented opposite to the first pair, reverses the aberration and leads to a sharp true sided image of any small (virtual) source at the initial focal point. Thus unlike *normal* neutron guides, even elliptic ones, the *Selene* guide does not have a rectangular cross-section, but is open with an L-shape. (For interpretation of the references to color in this figure caption, the reader is referred to the web version of this paper.)

Only a small fraction of the transported neutrons are actually focused [8] and the beam leaving these guides is divergent right behind the exit. However, an adequate design can lead to an intensity concentration on a relatively small area [9,10]. These elliptic guides allow larger beam cross-sections, wider divergence and they show less (if any) chromatic effects. The prize one has to pay is that the sample is strongly over-illuminated. Stopping all the unwanted neutrons (more than 99%) by absorbers behind the guide exit and before the sample leads likely to a high background and to radiation issues.

3. *Selene* guide as an add-on for Amor

3.1. The demonstrator

Full-scale *Selene* neutron guides (from source to sample) were discussed for a potential guide upgrade at PSI and for various instruments at the European Spallation Source (ESS) under construction in Sweden. To validate the concept and to learn about alignment and measurement procedures we constructed a down-scaled demonstrator of the *Selene* guide. The actual dimensions and the resulting performance of the guide as given in Table 1 were obtained by optimisation to the space and wavelengths available at the test beamline BOA at PSI.

The demonstrator was developed at PSI, fabrication including coating was performed by SwissNeutronics.

After some initial tests on BOA, the guide support was strongly simplified and the full guide was mounted on one aluminium beam with the possibility to vary horizontal and vertical inclination. This allowed us to continue the tests on the TOF reflectometer Amor at PSI (see below). The results encouraged us to modify Amor and to construct a spin polariser and an RF flipper, so that the demonstrator can be used as an add-on for user operation.

3.2. The TOF-reflectometer Amor

Amor was built as a very flexible reflectometer which optionally allows for measurements on liquid surfaces [11]. As it is hosted at a continuous neutron source (SINQ is a spallation neutron source with a frequency of 50 MHz) a pair of choppers is installed right after the neutron guide exit. This allows for a constant σ_λ/λ operation [12].

Besides a slit behind the chopper housing and the frame-overlap mirror, all optical and mechanical components are mounted on an 8 m long granite block, acting as an optical bench. In the conventional setting these components are (along the beam): reflecting polariser or deflector/slit 2/horizontally focusing parabolic guide segment[2]/slit 3/sample stage/slit 4/analyser/and slit 5 in front of the detector. The detector (optionally 0- or 2-dimensional) is mounted in a way that its composite movement (inclination, horizontal and vertical translation) describes an arc around the sample position.

With this set-up one can reach a q_z-range up to 0.3 $Å^{-1}$ (limited by the maximum detector angle). The resolution can be tuned, but in almost all cases $\sigma_{q_z}/q_z \approx 4\%$ is chosen.

The area-sensitive wire detector has an active area of 180 × 180 mm^2 The intrinsic spatial resolution is $\sigma_z \approx 1.2$ mm, but the data are binned with 128 × 256 channels. Each event is discretized into a (t, y, z) channel and counted in a histogram memory. Only after the measurement the data array is transferred to the computer, stored in the nexus format [13] and available for further processing. The storing process takes 6–10 s.

3.3. Modifications

The use of the demonstrator guide on Amor was restricted by the fact that a *Selene* guide causes a parallel offset of the beam, both horizontally and vertically. The vertical offset could be realised by translation stages which are otherwise used to measure with an inclined beam. But for the horizontal offset of 104.7 mm, the granite block had to be mounted on a motorised translation system so that a fast switching between the normal operation geometry and the *Selene* add-on is possible.

For the time being, the first slit directly behind the chopper housing, is used as virtual source. The subsequent components up to slit 3 have to be removed to provide space for the *Selene* guide. Thus an other way to polarise and flip the beam had to be implemented.

3.4. Constraints

The geometry of Amor and the beam characteristics at the end of the guide feeding the chopper impose some constraints. Slit 1 is located 1600 mm from the end of the guide, which has a cross-section of 50 × 50 mm^2. Thus the maximum divergence after the virtual source is 1.8°, which just illuminates the *Selene* guide. In addition, beams with a high angle relative to the Amor guide axis did undergo multiple reflections (up to 8 vertically and up to 17 horizontally due to the split guide geometry) and are thus of lower intensity.

The coating of the Amor guide is of $m=2$, which means that the full 1.8° divergence is obtained for $\lambda > 3.8$ Å, which matches the *Selene* guide's acceptance of 4 Å.

The area detector has a spatial resolution of $2\sigma_z \approx 2.5$ mm. To still obtain a high angular resolution, the detector is moved as far back on the optical bench as possible, i.e. ≈4 m from the sample. This results in a relatively high wavelength resolution $\sigma_\lambda/\lambda \approx 2.3\%$. To avoid frame overlap due to the longer flight path, the chopper frequency has to be reduced to 33 Hz (instead of the normal 50 Hz).

The *Selene* guide can accept neutrons from a region of ≈2 × 2 mm^2 in the plane of the virtual source. Thus the maximum footprint width on the sample is only 2 mm.

3.5. Optics

3.5.1. Polariser

A new type of polariser was designed for the *Selene* set-up on Amor, which makes use of the facts that the beam to be polarised originates from a small area and that far from the origin it has locally a small divergence.

We choose a supermirror-based polariser operated in transmission. To ensure the same angle of incidence for all beam trajectories, the polariser is bent to form a logarithmic spiral

Table 1
Basic geometrical parameters and derived properties of the demonstrator guide.

Source-sample distance	$4c$	4000 mm
Half-axes ratio	b/a	0.021480
Normalised length	ξ	0.60
Divergence	$\Delta\theta$	1.8° × 1.8°
Horizontal and vertical inclination	$\epsilon_{y,z}$	1.50°
Parallel offset		104.7 mm
Maximum spot size	$\Delta y \times \Delta z$	2 × 2 mm^2
Coating	m	2.5
Critical wavelength	$\lambda_{\min}$	4 Å

[2] This focusing guide concentrates the flux onto a 10 mm wide spot with 3 times the unfocused intensity.

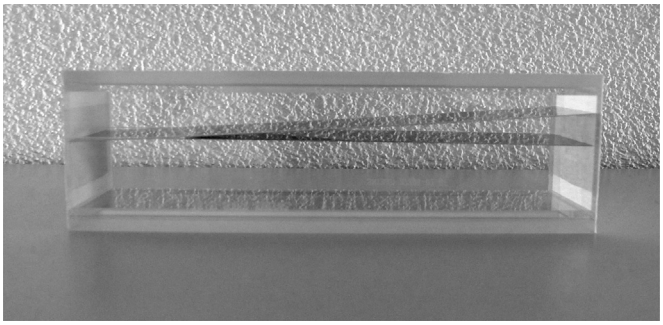

Fig. 2. Photo of the polariser and frame-overlap mirror based on transmission through equiangularly curved coatings. The glass tube is 215 mm long and has an inner height and width of 50 × 50 mm^2. The virtual source is to be 170 mm before the entrance (to the left). The device was produced by SwissNeutronics.

(equiangular spiral) with its pole at the beam origin. Since the *Selene* guide already starts 400 mm behind the virtual source, the space is rather limited, so that the actual polariser consists of two spirals with opposite sense of curvature, forming a V-shape. The coating, an $m=4.2$ Fe/Si supermirror, is applied to both sides of the substrates, 40 mm wide and 240 mm long Si-wavers. The spiral shape is defined by corresponding grooves in the inner sides of the rectangular glass-tube used as housing (see Fig. 2). To ensure a high polarisation efficiency, the device is mounted within a magnetic field of $H=400$ Oe, realised with permanent magnets.

The spin can be flipped with an RF flipper positioned behind the first guide segment.

3.5.2. Virtual source

Since the *Selene* guide acts as a 3-dimensional imaging optics, one can back-project the required beam footprint on the sample to the virtual source position. A diaphragm (an assembly of absorbing blades) with the shape, size and orientation of this projection is used at this position to define a *luminous field* being mapped to the sample.[3] For a perfectly aligned aperture and *Selene* guide only slight distortions occur due to gravitational aberration and remainders of coma aberration. No further optics is needed in this case.

The reality is that our first version of a luminous-field diaphragm is not precise and reliable enough, thus it is not used at present. A new device is being planned.

3.6. Set-up

Fig. 3 shows a CAD image of Amor with the *Selene* guide installed. The complete guide is mounted on an aluminium beam, which is hosted on a carriage on the optical bench. This and all the following components can be positioned along the instrument axis individually.

It is worth noting that there is a relatively wide free space around the sample as the guide ends 400 mm up stream. The motorised (bulky) slit 3 can be replaced for a thin fixed slit (if needed at all) and thus sample environment with a radius of 390 mm can be used. This is enough for a horizontal 7 T magnet or a sputter chamber for in-situ sample preparation.

3.6.1. Alignment of the Selene guide

For the alignment of the individual reflectors (in total 8 with a length of 600 mm, each) relative to each other, and of the full guide on the optical bench of Amor, we use optical light. Up to now

[3] In optical microscopy the analogue is called luminous-field diaphragm, field diaphragm or (if quasi circular) iris diaphragm. We adapted the first term since it illustrates best the purpose of the device.

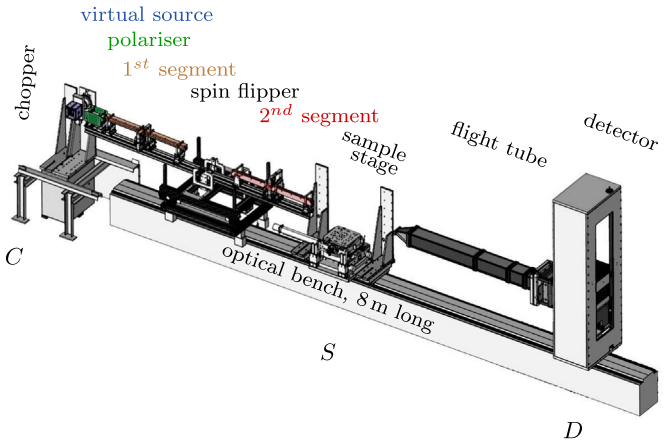

Fig. 3. CAD image of Amor showing the set-up with the *Selene* guide, the related optics, and the flight tube in front of the detector. *C*, *S* and *D* indicate the locations of the chopper, the sample and the detector, respectively.

white light is provided by an LED spotlight. A pinhole of 0.5 mm diameter defines the initial focal point. The reflector elements are then mounted and adjusted one-by-one in a way that the light emerging from the pin-hole is focused to the intermediate or final focal points, respectively. Even tiny deviations of the alignment lead to a broadening of the spots in the focal plane, or to a stripe-pattern of the spot on a screen before or behind the focal planes.

The orientation of the horizontally and vertically reflecting elements relative to each other should be 90°. This can be checked by looking at the joint of both: the double-reflected image of ones pupil should be round. Any compressed or elongated shape is a result of a too large or small angle, respectively. The 90° alignment leads to the diagonal dark line in the $I(y,z)$ map shown in Fig. 4. Besides some imperfections of the mirrors along the joint, this is caused by the parallaxes error the first reflection on the guide element introduces for the second reflection [14]. An optimisation of the angle is possible for short devices (relative to the focal point distance) as with Montel optics used at synchrotron beamlines. For long devices the optimisation in the entrance region is in conflict with the optimisation of the exit region.

With this alignment method a beam-spot size at the sample position below 1 mm in diameter can be reached. For the near future it is foreseen to replace the LED/pin-hole arrangement by a LASER/optics set-up creating a virtual point source in the μm−range. The screens will be replaced by an assembly of a

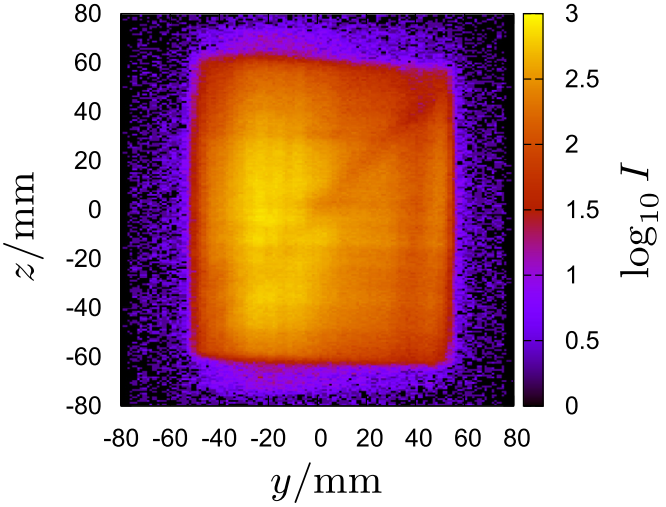

Fig. 4. Intensity map of the direct beam (without sample, $\gamma_D=0°$) on the detector, integrated over all wavelengths.

refraction-free beam splitter and two cameras in the focal plane and 15 cm behind it, respectively.

3.7. Limitations and areas of application

At the moment there is no spin analyser available for the focusing beam set-up on Amor. Thus spin-flip scattering cannot be investigated.

The present polariser (see Section 3.5) also acts as frame-overlap filter. For unpolarised measurements this means that there is no filtering of long wavelengths, which might lead to increased background at short wavelengths, i.e. high q_z. In the experiments performed so far this was not of relevance.

The *Selene* guide transports only neutrons coming from the close vicinity of the initial focal point. This has the effect that the maximum width of the footprint on the sample is only about 2 mm wide. Without the luminous-field diaphragm the maximum length of the footprint is restricted to 2 mm/ $\tan\theta$. With down to 24 mm this exceeds most of the samples measured on Amor even for highest possible θ.

The maximum detector angle γ_D of Amor is 8°, and the minimum wavelength transported by the *Selene* guide is 4 Å. This leads to an upper limit of $q_z \approx 0.23$ Å^{-1}.

The beam reaches the sample position horizontally. Measurements on liquid/liquid or liquid/gas interfaces are thus not possible in the standard configuration. A reflector behind the guide exit to bend down (or up) the beam is not yet realised.

Positively phrased, the *Selene* set-up works best for solid state samples with a small surface area, or where only a restricted area should be illuminated. For typical samples of 10 mm width the counting time is reduced by a factor 5 compared to the normal set-up on Amor already using a horizontal focusing.

The relatively short counting times together with the space around the sample enable time-resolved in-situ or in-operando studies. The highest time resolution reached up to now was about 1 min to cover $q_z \in [0.005, 0.07]$ Å^{-1}. Prominent reflectivity peaks at low q_z would allow for even shorter counting times.

4. Data acquisition and reduction

4.1. Sample alignment

Fig. 5 shows the geometrical situation at the sample in the scattering plane together with the nomenclature used here.

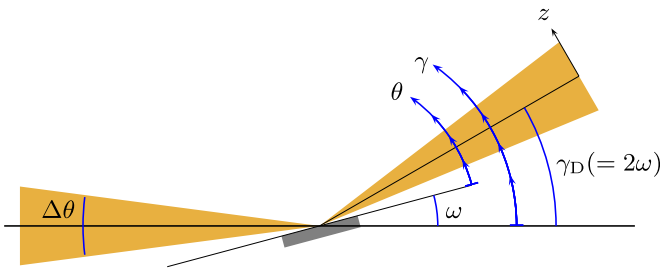

Fig. 5. Sketch of the sample geometry in the scattering plane. The yellow area shows the incoming and reflected beam, both with the divergence $\Delta\theta$. The inclination of the sample relative to the centre of the incoming beam (here identical to the instrument horizon) is called ω, and the respective angle of the reflected beam relative to the same axis is γ. In general the detector centre is located at $\gamma_D = 2\omega$. These are *instrument coordinates* and should not be confused with the situation on the sample, where the take-off angle of an individual neutron trajectory is called θ. While related to the instrument settings (see Fig. 6 (g)), this is the only relevant angle for data analysis. (For interpretation of the references to color in this figure caption, the reader is referred to the web version of this paper.)

Neither ω nor 2θ are well defined with a convergent beam anymore and thus *new* angles and definitions are introduced.

The focusing of the beam leads to an unfamiliar behaviour: As long as the sample surface is in the beam, the total reflection plateau will show up as a triangle in the $I(\lambda,\theta)$ map (see Fig. 7(j)), even for an angular misalignment of up to 1°. The challenge is to bring the sample to the focal point with an accuracy better than 0.1 mm.

Whenever possible we use white light coupled into the neutron beam path to actually see the focal spot. In these cases it is also possible to roughly align $\omega = \gamma_D/2$ by looking for the light reflected off the sample. In other cases one has to scan the sample through the beam until the mentioned triangle shows up. Probably this has to be repeated with a different ω, where the steps in ω are of the order of 0.5°.

Once one gets the wanted signal in $I(\lambda,\theta)$, one can precisely adjust ω. It is correct, when the inclined side of the triangle, which corresponds to the critical q_z, points to the origin ($\lambda = 0$ Å, $\theta = 0°$). In the final step the sample is scanned through the focal spot to find the best (most intense and homogeneous) illumination.

Our experience is that a misaligned ω can be easily corrected for after the measurements, but a shifted sample requires an equally shifted reference (see below) to ensure a correct data reduction.

The alignment normally is performed at a detector position of $\gamma_D = 2.2°$ and $\omega \approx 1.1°$ where there is no overlap with the non-reflected beam but still relatively high intensity due to the small q_z.

4.2. Measurement

For the measurement the required q_z-range determines the ω and $\gamma_D (= 2\omega)$ settings. Taking the actual λ- and θ-dependence of the incoming beam on Amor into account one can estimate the sample inclination based on the lower q_z limit with $\omega \approx 0.9° + \arcsin q_l \cdot 0.95$ Å and the corresponding upper q_z limit is then $q_u \approx 2.8 q_l + 0.09$ Å^{-1}. For most applications the angles $\omega = 1.1°$ and 3.6° are sufficient to cover $q_z \in [0.004, 0.23]$ Å^{-1}.

The counting times vary between a minute for relatively large samples (40 mm long) and time-resolved studies at small q_z, and several hours for samples of 5 mm length and $q_z \in [0.005, 0.23]$ Å^{-1}.

Each measurement results in a histogram $\mathbf{H}_{raw}$ with entries $H_{raw\ ijk}$ = counts in time interval i and detector pixel jk, the one-dimensional arrays for time $\mathbf{t}$ and the detector coordinates $\mathbf{z}$ and $\mathbf{y}$, and the monitor signal n_{mon}. The latter replaces the counting time because the neutron beam flux at SINQ is not constant, but changes on a split-second time-scale. Thus the beam intensity before the chopper is monitored. So the intensities $I = H/n_{mon}$ discussed below are of the dimension counts per monitor signal, rather than counts per second.

4.2.1. Reference

To reduce and to normalise $\mathbf{H}_{raw}$ a known reference sample is used, measured under similar conditions. Ideally this reference has the same dimensions as the sample and a high reflectivity. We use an $m = 5$ Ni/Ti supermirror[4] (SM) with a known reflectivity $R^{SM}(q_z)$. It is measured at $\omega \approx 1.1°$ ($\mathbf{H}^{SM}$) and at 3°. The first angle ensures that the full λ-θ-range corresponds to a $q_z < q_z^{c,SM}$, the second measurement showing the critical edge $q_z^{c,SM}$ is used to cross-check ω.

[4] The number m relates the critical q_z of the supermirror to that of natural Ni.

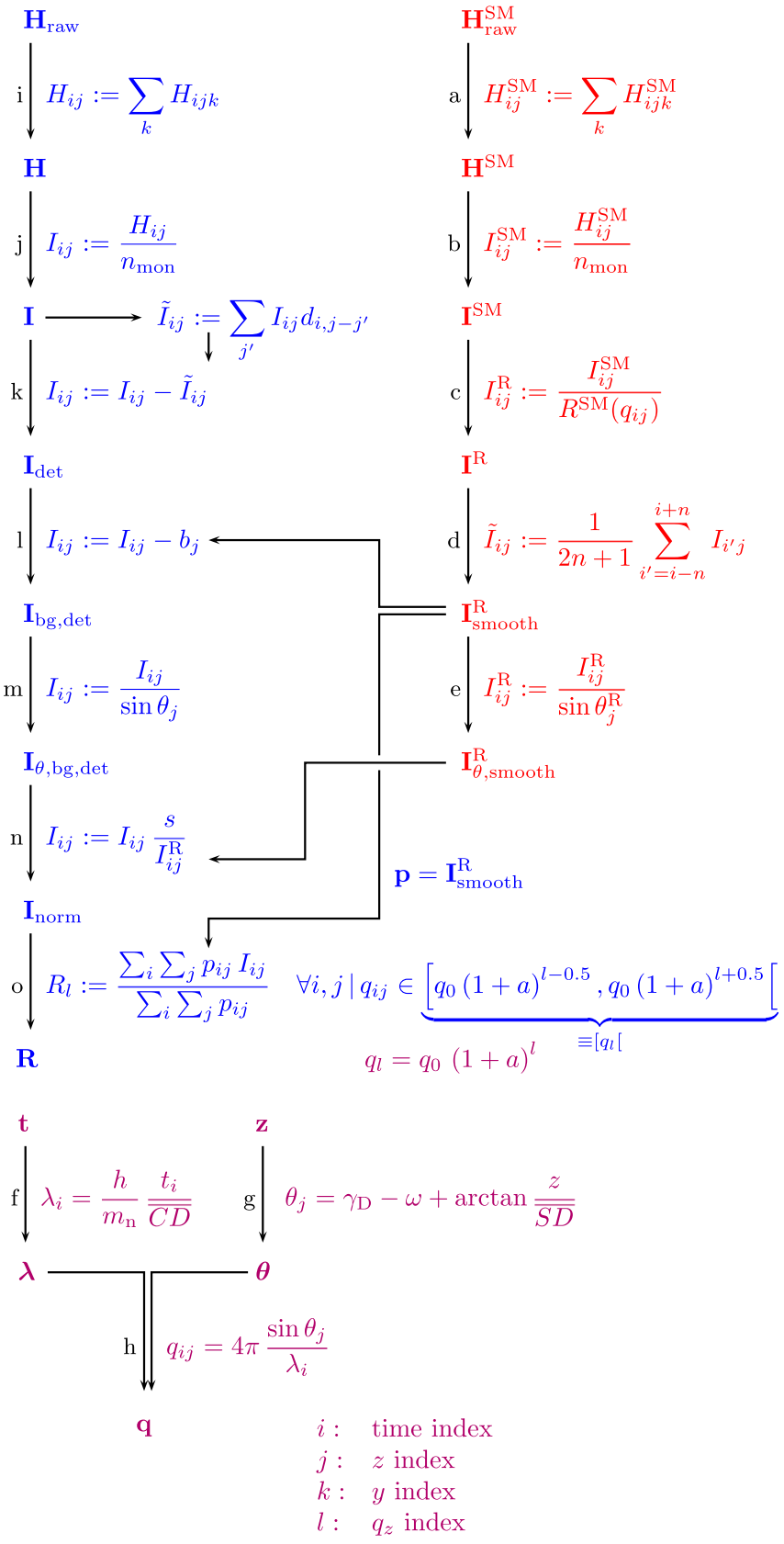

Fig. 6. Flow chart (simplified) of the data reduction process. The first column (blue) corresponds to the sample measurement, here **H** means histogram, **I** means intensity and **R** reflectivity. Bold symbols stand for data arrays, where the array elements have the indices i,j,k and l, referring to time, detector z coordinate, detector y coordinate and q-bin, respectively. The second column (red) corresponds to the reduction of the supermirror measurement ($^{\mathrm{SM}}$) to obtain the reference ($^{\mathrm{R}}$). On the right the connection of the histogrammed time- and position-data and the parameters wavelength λ and reflection angle θ and finally momentum transfer q are given. The first row contains the raw data stored in the measurement file. The small letters refer to the related entries in the text. (For interpretation of the references to color in this figure caption, the reader is referred to the web version of this paper.)

4.3. Data reduction

To obtain the reflectivity $R(q_z)$ (or more precise the one-dimensional reflectivity array **R**) from the measured histogram **H** the latter has to be corrected for influences of the scattering geometry and the intensity distribution of the incoming beam. In addition, background originating from the instrument and its environment can be subtracted.

In this section the essential data reduction steps are discussed briefly. Fig. 6 shows a simplified flow chart of the reduction process. The correction is indicated by a subscript. In parallel to the shown steps, a full error handling is performed.

Fig. 7 shows intensity maps for some of the data arrays obtained during the reduction and the final reflectivity for the example presented in Section 5.

4.3.1. Reference

The reference measurement data enter the reduction process in three different ways: it gives an estimate for the background **b**, allows for the normalisation of the intensity array **I** and delivers the weighting factors **p** for the projection of the latter onto a q_z-grid.

The reduction process for the reference is summarised in the second column of Fig. 6. It essentially consists of

(a) Projection of the three-dimensional histogram $\mathbf{H}^{\mathrm{SM}}_{\mathrm{raw}}$ onto the two-dimensional $\mathbf{H}^{\mathrm{SM}}$.
(b) Normalisation by the monitor counts n_{mon} to get the intensity array $\mathbf{I}^{\mathrm{SM}}$.
(c) Normalisation by the reflectivity of the supermirror $R^{\mathrm{SM}}(q)$ resulting in the total intensity incident on the reference $\mathbf{I}^{\mathrm{R}}$.
(d) Smoothing along the time coordinate to reduce the statistical noise. This is justified by the expected smoothness of R^{SM} below the critical edge and of the neutron spectrum.
(e) Illumination correction, taking into account the sample size projected onto the detector (see Fig. 7(e)).

For some correction steps the wavelength, the reflection angle or q_z are needed. The respective formulae are given in the right part of Fig. 6:

(f) Calculation of the wavelength from the histogramming time-steps **t** using the chopper-detector distance $\overline{CD}$, the Planck constant h and the neutron mass m_{n}.
(g) Calculation of the reflection angle θ from the detector angle γ_{D}, the sample orientation ω, the sample-detector distance $\overline{SD}$ and the z-position on the detector.
(h) Association of a q_z with each bin, resulting in a two-dimensional array **q**.

4.3.2. Sample

The first reduction steps for the sample are similar to the ones for the reference. The essential steps are displayed in the first column in Fig. 6.

(i) Projection of the three-dimensional histogram $\mathbf{H}_{\mathrm{raw}}$ onto the two-dimensional **H**.
(j) Normalisation by the sample monitor counts n_{mon} to give the intensity array **I** (see Fig. 7(j)).
(k) Correction of the spatial detector response function. The Al window of the detector scatters a fraction of the incoming neutrons and thus leads to a halo decreasing exponentially with distance r around each irradiated point [15, Fig. 10 and discussion]. In principle $\mathbf{H}_{\mathrm{raw}}$ has to be deconvoluted with a λ-dependent response function. We chose the simplified approach to subtract the measured array **I** convoluted with d

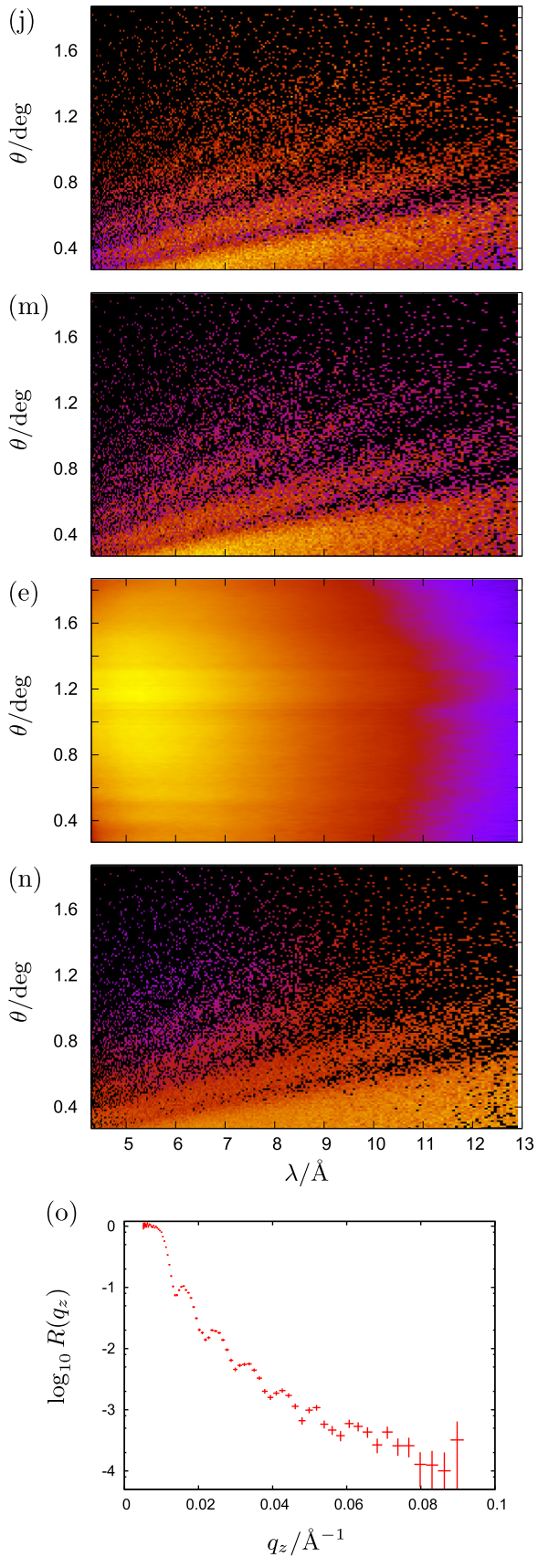

Fig. 7. Illustration of the essential reduction steps. The numbering corresponds to the one in the text and in Fig. 6. (j) intensity as detected (**I**) and (m) after θ-correction ($\mathbf{I}_{\theta,\mathrm{bg,det}}$). (e) θ-corrected reference measurement. (n) reflectivity $\mathbf{I}_{\mathrm{norm}}$. (o) reflectivity **R** after projection onto a q_z grid.

(λ, z) describing the wings of response function. $d(\lambda, z)$ was obtained from fits to measurements.

The difference between the two blue lines in Fig. 11(a) tells the order of magnitude of this correction.

(l) Background subtraction. Background coming from the sample or (in the case of over-illumination) from its environment due to incoherent scattering has the time-characteristics of the incident beam, but only a weak θ dependence. To estimate the background $b(\lambda)$ the reference measurement is summed over θ and scaled with a factor b':

$$b_j = b' \sum_i I^{\mathrm{R}}_{ij} + b''$$

b' and a time-independent contribution b'' (due to external sources or activated components) can be determined e.g. by measurements with $\omega < \gamma_{\mathrm{D}}/2 - \Delta\theta/2$, or by fitting.

(m) Illumination correction analogue to (e), but probably with a different $\boldsymbol{\theta}$ (see Fig. 7(m)).

(n) Normalisation to the wavelength-dependent flux incident on the sample. This is achieved via pixel-by-pixel normalisation of $\mathbf{I}_{\theta,\mathrm{bg,det}}$ with $\mathbf{I}^{\mathrm{R}}_{\theta,\mathrm{smooth}}$. A scaling factor s takes differences of sample and reference size into account and it can correct for the unstable monitor efficiency on Amor[5] (see Fig. 7(n)).

(o) In the last step the two-dimensional reflectivity array $\mathbf{I}_{\mathrm{norm}}$ is projected onto a defined q_z-grid. By default a logarithmic grid is used with a resolution of $q_{l=0} = 2e^{-3}$ Å^{-1}. The weighting factors for the summation are the entries of the reference array $\mathbf{I}^{\mathrm{R}}_{\mathrm{smooth}}$ before the illumination correction. The reason is that otherwise the low-θ region with relatively low statistics (due to the small angle of incidence) would be overemphasised.

Steps (e), (m), (n) and (o) can be summarised as

$$R_l := \frac{\sum_{ij} \frac{\sin\theta^{\mathrm{R}}_j}{\sin\theta_j} I_{\mathrm{bg,det}\ ij}}{\sum_{ij} I^{\mathrm{R}}_{\mathrm{smooth}\ ij}} \quad \forall i,j \mid q_{ij} \in [q_l[\tag{1}$$

4.3.3. Resolution

The problem with the approach to sum over equal q_z intervals (Fig. 6(o)) is that the resolution varies over $\mathbf{I}_{\mathrm{norm}}$.

The wavelength resolution is given by the double-blind chopper system [12] of Amor and its distance to the detector. The pulse has an almost rectangular shape. For the *Selene* set-up one gets $\Delta\lambda/\lambda = \overline{C_1C_2}/\overline{CD} \approx 5.8\%$, here. $\overline{C_1C_2} = 490$ mm is the distance between the first and second chopper disks. This corresponds to $\sigma_\lambda/\lambda \approx 2.3\%$.

The angular resolution is given by the spatial resolution of the detector with FWHM $\Delta z \approx 2.5$ mm and the sample-detector distance $\overline{SD} \approx 4$ m:

$$\sigma_\gamma = \frac{1}{2\sqrt{2\ln 2}} \arctan\frac{\Delta z}{\overline{SD}} \approx 0.016^\circ \tag{2}$$

For larger samples (length x_{S}) and high angles the projected size of the footprint might be of the same order or larger than the detector resolution. This leads to

$$\sigma_{\theta\, j} = \sqrt{\sigma_\gamma^2 + \left(\frac{1}{2\sqrt{2\ln 2}} \arctan\frac{x_{\mathrm{S}} \sin\theta_j}{\overline{SD}}\right)^2} \tag{3}$$

The resulting q_z-resolution is

$$\frac{\sigma_{qij}}{q_{ij}} \approx \sqrt{\left(\frac{\sigma_{\lambda\, i}}{\lambda_i}\right)^2 + \left(\frac{\sigma_\gamma}{\theta_j}\right)^2 + 0.18\left(\frac{x_{\mathrm{S}}}{\overline{SD}}\right)^2} \tag{4}$$

[5] The monitor efficiency on Amor varies by up to 10% on a time scale of several hours.

Fig. 8 shows calculated σ_q/q_z curves as a function of θ. While the sample size has only a minor influence, the detector resolution spoils the q_z-resolution for small θ. Taking this into account, the measurements should be performed at an ω as high as possible, but still covering the interesting q_z-range. Optionally one can evaluate the scaling factor s from total reflection by using the full θ-range, and then repeat the summation with a reduced range to get higher resolution.

The q_z resolution for each entry in the reflectivity array $\mathbf{R}$ is obtained analogue to step o in Fig. 6:

$$\sigma_{q_l} := \frac{\sum_{ij} p_{ij}\, \sigma_{q\ ij}}{\sum_{ij} p_{ij}} \quad \forall i,j \mid q_{ij} \in [q_l] \tag{5}$$

Fig. 11 illustrates the validity of these considerations by comparing measured data to simulations taking into account only the wavelength resolution or the resolution obtained by Eq. (5).

In the case of a curved sample surface the reflection for each incoming θ gets blurred on the detector, which might dominate the resolution and render a useful data analysis impossible. In this case the wide divergence provided by the *Selene* guide cannot be used, but must be restricted with slits at the guide exit.

R. Cubitt recently published a similar approach for data reduction for cases when the detector is used to determine θ [16]. The essential difference is that there a flat $I(\theta)$ distribution over the incoming beam is assumed and no reference sample is used.

5. Example: in-situ annealing

The example of in-situ annealing for the investigation of Li diffusion in Si is used here to illustrate some of the reduction steps discussed above and the performance of the *Selene* guide. The data are courtesy of E. Hüger and H. Schmidt, Technical University of Clausthal, Germany.

This experiment was chosen because the required time-resolution and the measurement time on Amor match. These measurements [17] were performed with an unpolarised beam. The counting time per reflectivity reached down to 90 s. A special annealing chamber based on the system AO 500 by MBE Komponenten was build to fit on the sample stage of Amor (see Fig. 9).

The samples were multilayers of the type ^{6}LiNbO$_3$/[Si/^{7}LiNbO$_3$/Si/^{6}LiNbO$_3$]$_5$/Si with equal thicknesses of the respective

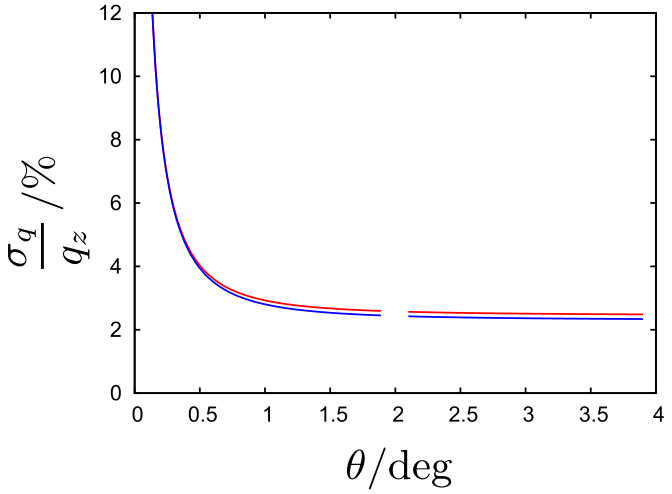

Fig. 8. Resolution σ_{q_z}/q_z as a function of θ for sample length of l=40 mm (red curves) and 10 mm (blue curves), respectively. A wavelength resolution of σ_λ/λ = 2% was assumed and a sample-detector distance $\overline{SD} = 4$ m. The curves correspond to ω=1° and 3°, respectively. (For interpretation of the references to color in this figure caption, the reader is referred to the web version of this paper.)

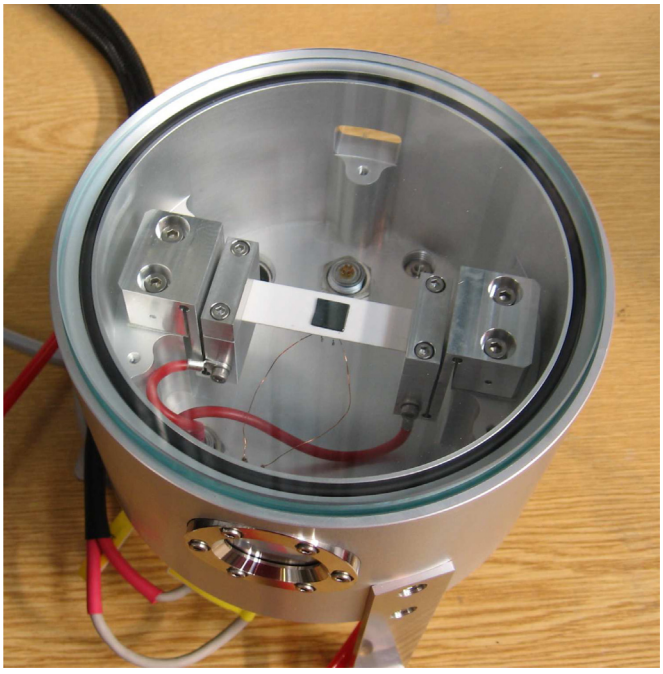

Fig. 9. Furnace for in-situ/in-operando annealing. The beam enters and leaves the recipient through sapphire windows. The 1 cm^2 sample is visible as a dark square on the white resistive heater bar.

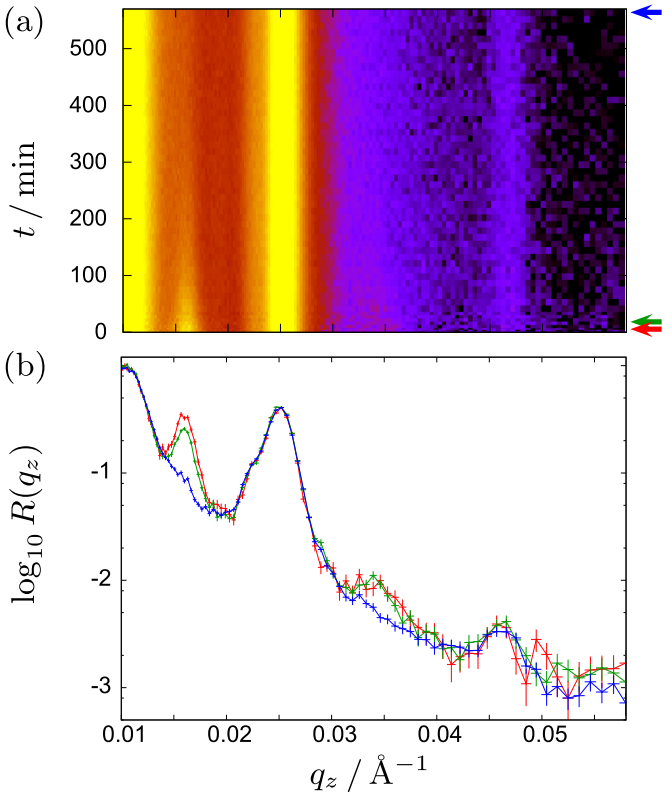

Fig. 10. (a) Intensity map $R(q_z)$ as a function of annealing time (in minutes) for a multilayer of $[^6Li_3NbO_4/Si/^7Li_3NbO_4/Si]_5/Si$. The colour scale is non-linear and was adapted to highlight the interesting features. (b) Selected $R(q_z)$ curves from this map measured at $t=0\rightarrow3$ min (red), $t=18\rightarrow24$ min (green) and $t=558\rightarrow570$ min (blue). (For interpretation of the references to color in this figure caption, the reader is referred to the web version of this paper.)

Si or $LiNbO_3$ layers [18,19]. The strong contrast at the chemical interfaces leads to a pronounced Bragg peak in the reflectivity curve. The contrast between the two Li-containing layers is much weaker. The doubled period results in a small Bragg peak in between the total reflectivity plateau and chemical Bragg peak. Upon annealing the diffusivity of Li through Si is increased, which leads to an assimilation of the $^6Li/^7Li$ ratios and thus to a decrease of the corresponding Bragg peak. The lithium permeability (solubility × diffusivity) describing the transport through the silicon layer can be derived from the Bragg peak decrease [17–19]. From the temperature (in the range 80–380 °C) and the measured time constant of the decrease (6–60 min) one can extract the activation energy of the mobility of Li in Si.

For the actual measurement the sample was mounted and aligned, then a reflectivity measurement was performed before annealing and then every 90 s during annealing. I.e. the sample was not cooled down for measurements.

Fig. 10 shows a typical intensity map of $R(q_z)$ vs. q_z and annealing time t for these kind of measurements, together with some selected $R(q_z)$ curves. The decrease of the Bragg peak associated with the isotope contrast (at $q_z \approx 0.16$ Å^{-1} and higher orders at 0.34 Å^{-1} and 0.57 Å^{-1}) is nicely visible. The chemical Bragg peaks stay unchanged.

On an other sample of similar composition a series of measurements have been performed with much better statistics in order to illustrate some of the aspects discussed in Section 4.3. Fig. 11(a) shows the reflectivity curves for $\omega=1.0°$ with and without the correction for the detector response function, the simulated reflectivity taking only the wavelength resolution into account and the resolution σ_q/q obtained from the experimental data using Eq. (5). It is obvious that ignoring the detector resolution in the simulated data leads to a wrong result for $q_z < 0.04$ Å^{-1}. The red lines in Fig. 11(b) and (c) are the simulated reflectivity convoluted with a Gaussian function using the experimental $\sigma_q(q)$ displayed in (c). The experimental data collected at $\omega=3.0°$, shown in (b), were merged with the ones in (a) to give the curves shown in (c).

6. Outlook

For the near future we plan to improve the alignment procedure for the *Selene* guide and for the sample, respectively. The latter involves sample environment that allows for a better access to the sample and for a reliable and stable sample position.

A spin analyser also based on the equiangular spiral concept is in planning.

The resolution issue for small θ and the time loss during data download from the histogram memory can be solved with a detector with higher spatial resolution in the scattering direction $\Delta z < 0.5$ mm and faster electronics (integral count rate 10^4 s^{-1} for the demonstrator, $>10^5$ s^{-1} for a full scale guide allowing for larger footprints).

On the longer time scale the complete guide feeding Amor might be replaced by a *Selene*–type guide. Depending on the spatial constraints either the moderator or a pin-hole several meters downstream of it will form the initial focal point. The final focal point again defines the sample position. The granite beam will have to be moved towards the moderator by several meters and tilted. Fig. 12 shows sketches of the present and the planned guide layout. Assuming the divergence and transmission of the full guide to be the same as of the demonstrator, the gain is given by the omission of the old guide with its low transmission (only 20%) and inhomogeneous phase space (due to many reflections for

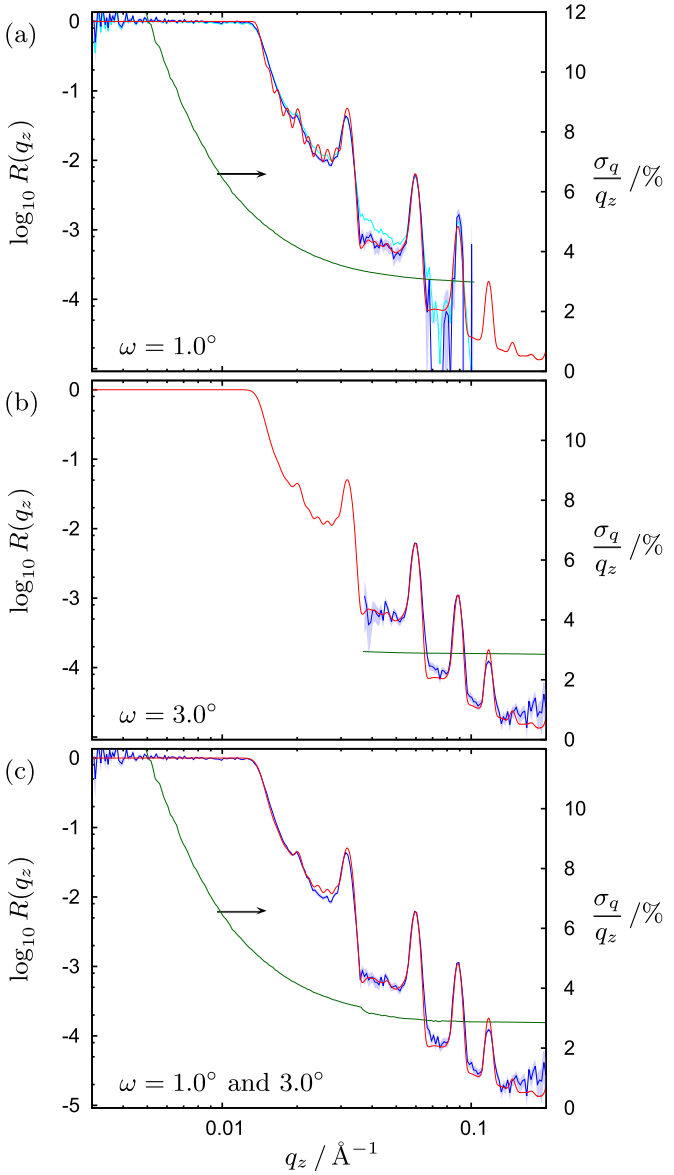

Fig. 11. Measured (blue with a pale blue error region) and simulated (red) reflectivities for a $LiNbO_3$/Si multilayer (after annealing) as discussed in Section 5. The green lines show the resolution σ_q/q_z and are related to the second y-axis. (a) Data set obtained at $\omega = 1.0°$ with (dark blue) and without (light blue, no error region) correction for detector response are discussed in Section 4.3.2(k). Simulated data convoluted with $\sigma_q/q = \sigma_\lambda/\lambda = 2.3\%$ to illustrate the influence of the detector resolution. (b) Data and resolution for $\omega = 3.0°$, the red curve is the simulated reflectivity convoluted with the expected resolution according to Eq. (5). (c) Merged corrected data sets for $\omega = 1.0°$ and $\omega = 3.2°$ and resolution. (For interpretation of the references to color in this figure caption, the reader is referred to the web version of this paper.)

higher angles). In addition the maximum reachable footprint increases from 2 mm to 15 mm. Thus the counting time will be reduced by a factor 35 for samples of at least 15 mm width, relative to the present demonstrator set-up. At the same time the radiation background in the experimental hall is expected to get lower because of the much reduced flux in the guide.

The European Spallation Source will host the neutron reflectometer *Estia* being developed and constructed by PSI [20]. *Estia* will be equipped with a *Selene* type neutron guide.

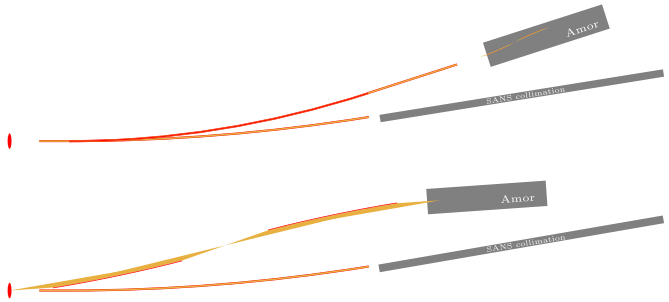

Fig. 12. Sketches to illustrate the actual (top) and planned guide lay-out (bottom) for Amor and the large Small Angle Neutron Scattering instrument at PSI. The gray bars correspond to the granite block for Amor (see Fig. 3) and to the collimation section for SANS, respectively.

7. Conclusion

We recapitulated the concept of using a focused beam and a position-sensitive detector for high-intensity specular reflectometry on a TOF reflectometer. The implementation of both, hardware and a data reduction algorithm on Amor at PSI were presented. The hardware is the combination of the 4 m long demonstrator of the *Selene* guide and a matched polariser with a equiangular spiral shape. Data reduction deviates from conventional measurements essentially in the use of a reference measurement and in the projection of wavelength and angle dependent data array onto a q_z grid. The performance was shown on the example of studies of Li diffusion through Si with a time resolution down to 90 s. The same experiment was used to illustrate the agreement between the calculated and the measured resolution function, respectively.

Acknowledgements

Particularly we thank E. Hüger, F. Strauß and H. Schmidt for providing the material for the experimental examples.

We thank U. Hansen, T. Panzner and P. Korelis for their help during the early tests and measurements with the *Selene* guide.

The *Selene* guide demonstrator was co-financed by the Swiss State Secretariat for Education, Research and Innovation SE RI, as an in-kind contribution to the development of *Estia* to the European Spallation Source ESS in Lund.

This work is based on experiments performed on Amor at the Swiss spallation neutron source SINQ, Paul Scherrer Institute, Villigen, Switzerland.

References

[1] J. Daillant, A. Gibaud, X-Ray and Neutron Reflectivity: Principles and Applications, Lecture Notes in Physics, Monographs 58, Springer-Verlag Berlin Heidelberg, New York, 1999.
[2] R. Cubitt, J. Stahn, Eur. Phys. J. Plus 126 (2011) 111.
[3] Frédéric Ott, Alain Menelle, Nucl. Instrum. Methods Phys. Res. A 586 (1) (2008) 23, Proceedings of the European Workshop on Neutron Optics—NOP '07.
[4] J. Stahn, T. Panzner, U. Filges, C. Marcelot, P. Böni, Nucl. Instrum. Methods Phys. Res. A 634 (1) (2011) Supplement, 1, Proceedings of the International Workshop on Neutron Optics NOP 2010, S12–S16, http://dx.doi.org/10.1016/j.nima.2010.06.221.
[5] J. Stahn, U. Filges, T. Panzner, Eur. Phys. J. Appl. Phys. 58 (2012) 4.
[6] F. Ott, A. Menelle, Eur. Phys. J.—Spec. Top. 167 (2009) 93.
[7] H. Maier-Leibnitz, T. Springer, J. Nucl. Energy Parts A/B 17 (1963) 217.
[8] L.D. Cussen, D. Nekrassov, C. Zendler, K. Lieutenant, Nucl. Instrum. Methods Phys. Res. Sect. A—Accel. Spectrom. Detect. Assoc. Equip. 705 (March) (2013) 121.

[9] C. Zendler, D. Nekrassov, K. Lieutenant, Nucl. Instrum. Methods Phys. Res. Sect. A—Accel. Spectrom. Detect. Assoc. Equip. 746 (May) (2014) 39.
[10] Leo D. Cussen, Thomas Krist, Klaus Lieutenant, Nucl. Instrum. Methods Phys. Res. Sect. A—Accel. Spectrom. Detect. Assoc. Equip. 777 (March) (2015) 6.
[11] M. Gupta, T. Gutberlet, J. Stahn, P. Keller, D. Clemens, Pramana—J. Phys. 63 (2004) 57.
[12] A.A. van Well, Phys. B: Condens. Matter 180–181 (2) (1992) 959.
[13] Mark Koennecke, Frederick A. Akeroyd, Herbert J. Bernstein, Aaron S. Brewster, Stuart I. Campbell, Bjoern Clausen, Stephen Cottrell, Jens Uwe Hoffmann, Pete R. Jemian, David Maennicke, Raymond Osborn, Peter F. Peterson, Tobias Richter, Jiro Suzuki, Benjamin Watts, Eugen Wintersberger, Joachim Wuttke, J. Appl. Crystallogr. 48 (February (1)) (2015) 301.
[14] Giacomo Resta, Boris Khaykovich, David Moncton, J. Appl. Crystallogr. 48 (April (2)) (2015) 558.
[15] J.E. Bateman, R. Dalgliesh, D.M. Duxbury, W.I. Helsby, S.A. Holt, C.J. Kinane, A. S. Marsh, N.J. Rhodes, E.M. Schooneveld, E.J. Spill, R. Stephenson, Nucl. Instrum. Methods Phys. Res. A 698 (January) (2013) 168.
[16] Robert Cubitt, Thomas Saerbeck, Richard A. Campbell, Robert Barker, Philipp Gutfreund, J. Appl. Crystallogr. 48 (December (6)) (2015) 2006.
[17] Erwin Hueger, Lars Doerrer, Johanna Rahn, Tobias Panzner, Jochen Stahn, Gerhard Lilienkamp, Harald Schmidt, Nano Lett. 13 (March (3)) (2013) 1237.
[18] E. Hueger, J. Stahn, H. Schmidt, J. Electrochem. Soc. 162 (2015) A7104.
[19] E. Hueger, L. Doerrer, J. Stahn, T. Geue, H. Schmidt, Defect Diffus. Forum 363 (2015) 49.
[20] Home-page of the instrumentation project Estia for the European Spallation Source, ESS: URL: ⟨https://psi.ch/lns/estia⟩.